Geophysical Journal International

Geophys. J. Int. (2012) **191,** 207–223 doi: 10.1111/j.1365-246X.2012.05598.x

Evidence for remotely triggered microearthquakes during salt cavern collapse

Philippe Jousset[1,2] and Jérémy Rohmer[1]

[1] *BRGM, RISK Division,* 3 *av. C. Guillemin, BP* 36009, 45060 *Orléans Cedex* 2, *France. E-mail: pjousset@gfz-potsdam.de*
[2] *GFZ Helmholtz Center, German Research Center for Geosciences, Telegrafenberg,* 14473 *Potsdam, Germany*

Accepted 2012 June 29. Received 2012 June 25; in original form 2011 November 30

SUMMARY

Microseismicity is a good indicator of spatio-temporal evolution of physical properties of rocks prior to catastrophic events like volcanic eruptions or landslides and may be triggered by a number of causes including dynamic characteristics of processes in play or/and external forces. We show evidence of triggered microseismicity observed in the vicinity of an underground salt cavern prone to collapse by a remote $M \sim 7.2$ earthquake, which occurred ∼12 000 km away. High-dynamic range broad-band records reveal the strong time-correlation between a dramatic change in the rate of local high-frequency microseismicity and the passage of low-frequency seismic waves, including body, Love and Rayleigh surface waves. Pressure was lowered in the cavern by pumping operations of brine out of the cavern. We demonstrate the near critical state of the cavern before the collapse by means of 2-D axisymmetric elastic finite-element simulations. On this basis, we show that the increment of stress necessary for the failure of the Dolomite layer, which ensures the stability of the whole system, is of the same order of magnitude as the maximum dynamic stress magnitude observed during the passage of the earthquakes waves. This suggests that the stress oscillations due to the seismic waves correlated with the recorded microearthquakes induced damage of the overburden, which eventually led to the collapse of the salt cavern. We show that the contribution of Rayleigh waves is the most efficient to trigger microseismicity at periods close to the natural fundamental frequency of the cavern system found at about 10–20 s by investigating the impulse response of the cavern + overburden + brine system.

Key words: Time series analysis; Earthquake dynamics; Broad-band seismometers; Earthquake interaction, forecasting and prediction; High strain deformation zone; Calderas.

1 INTRODUCTION

Correlated distant main shocks and triggering local seismicity activity have been observed and investigated in many contexts for over a decade (Velasco *et al.* 2008). Large remote earthquakes at distances ranging from several faults lengths to thousands of kilometres are known to induce or modulate seismic activity at volcanoes (Walter *et al.* 2009; Cannata *et al.* 2010), at geothermal systems (Ingebritsen & Rojstaczer 1996; Manga & Brodsky 2006), to trigger earthquakes (Brodsky & Prejean 2005), non-volcanic tremor (Miyazawa & Brosdky 2008), and slow slip event (Itaba & Ryosuke 2011). In this work, we investigate relationships between stress changes induced by seismic surface waves generated by the $M \sim 7.2$ Kepulauan Talaud earthquake (Indonesia; Table 1) and the occurrence of microseismicity around an unstable cavern prone to collapse. The cavern is located within the salt deposits of the Keuper epoch (Late Triassic period around 200 Ma, Bourquin *et al.* 1997) at the eastern edge of the Paris sedimentary basin, Lorraine, France (salt mining concession of Cerville-Buissoncourt).

The cavern was created through an original mining technique solution, known as 'channel and drilling' method (see Fig. 1). In a first step (Fig. 1a), an 'exploitation' channel (conduit of ∼1 km long and several meters thick) is created through dissolution of the rock salt layer (∼80 m thick at ∼200 m depth) by water injection through aligned exploitation wells (line denoted A and B in Fig. 2). In a second step (Fig. 1b), brine is extracted at one end of the line of exploitation wells and fresh water is injected at the other end leading to the formation of a cavern progressively growing and extending upwards. In early 2009, the brine-filled cavern has reached critical dimensions in terms of mechanical instability (e.g. Mercerat *et al.* 2010), and the mine operator decided to proceed to the collapse of the cavern overburden. This was achieved through pumping brine out of the cavern, which reduced the inner cavern fluid pressure. Its stability was mainly ensured by the Beaumont Dolomite (e.g. Nothnagel 2003; Mercerat *et al.* 2010), composed of an un-fractured, stiff dolomite of Young's modulus ∼79 GPa and anhydrite layer of Young's modulus ∼88 GPa (see Figs 1 and 2; Table 2). More than 12 500 m^3 of brine had to be pumped to

Table 1. GPS coordinates of the broad-band stations and of the $M \sim 7.2$ Kepulauan Talaud earthquake.[a]

	CE1	CE2	CE3	$M \sim 7.2$ Earthquake
Latitude	48.675361° N	48.675527° N	48.6775° N	3.902° N
Longitude	6.32025° E	6.324583° E	6.318278° E	126.4° E
Elevation/depth				20 km

[a]Seismic waves hit the network with an azimuth of 324° (see Fig. 2).

break the Dolomite and destabilize the overburden up to the final overburden surface collapse on 2009 February 13.

Mine monitoring uses mainly geophysical techniques (see ISRM 2008 for a review in the context of post-mining) including ground deformation (see e.g., Raucoules *et al.* 2003 for an illustration of both surface-based measurements and space-borne interferometry) and seismic monitoring (Ford *et al.* 2008). Within the GISOS framework (Scientific Grouping of Research Interest on the Impact and Safety of Underground Works), real-time monitoring geophysical multiparameter monitoring experiment (Daupley *et al.* 2010) of the cavern behaviour has been undertaken from its stationary state in fall 2004 to the surface collapse (Mercerat *et al.* 2010; Contrucci *et al.* 2011, Lebert *et al.* 2011).

In this work, we deployed three high-dynamic range broad-band seismometers from 2008 July to 2009 March, at less than 200 m from the cavern (Fig. 2). Broad-band seismology has been used at many sites including volcanoes (Neuberg *et al.* 1994; Surono *et al.* 2012; Jolly *et al.* 2012), geothermal systems (Jousset *et al.* 2011), tectonic environments (Jousset & Douglas 2007) and, to our knowledge for the first time, in a mining environment (Jousset *et al.* 2010). Advantages of broad-band seismology in mining environment are demonstrated in Section 2. We discuss criteria (Section 3) and possible mechanisms (Section 4) for remote triggering by modelling the stress state evolution during the brine pumping and by assessing the failure tendency of the Beaumont dolomite layer using the Mohr-Coulomb failure criterion.

2 OBSERVATIONS

2.1 Seismic network and experiment

Each of our three seismic stations (Table 1; Fig. 2) comprised a Güralp CMG-40TD (60 s) broad-band seismometer, a GPS antenna for synchronization between records at different stations, and a battery and solar panel for power supply. Data was sampled at 100 Hz and continuously stored on a local disk through a Güralp CMG-DCM data logger.

The pressure in the cavern was measured at the brine extraction wells (see Fig. 1) by the brine level height (measured in metres with reference being the general levelling of France, denoted NGF). On 2009 February 10 at ∼7:00 UTC, the pressure was lowered from

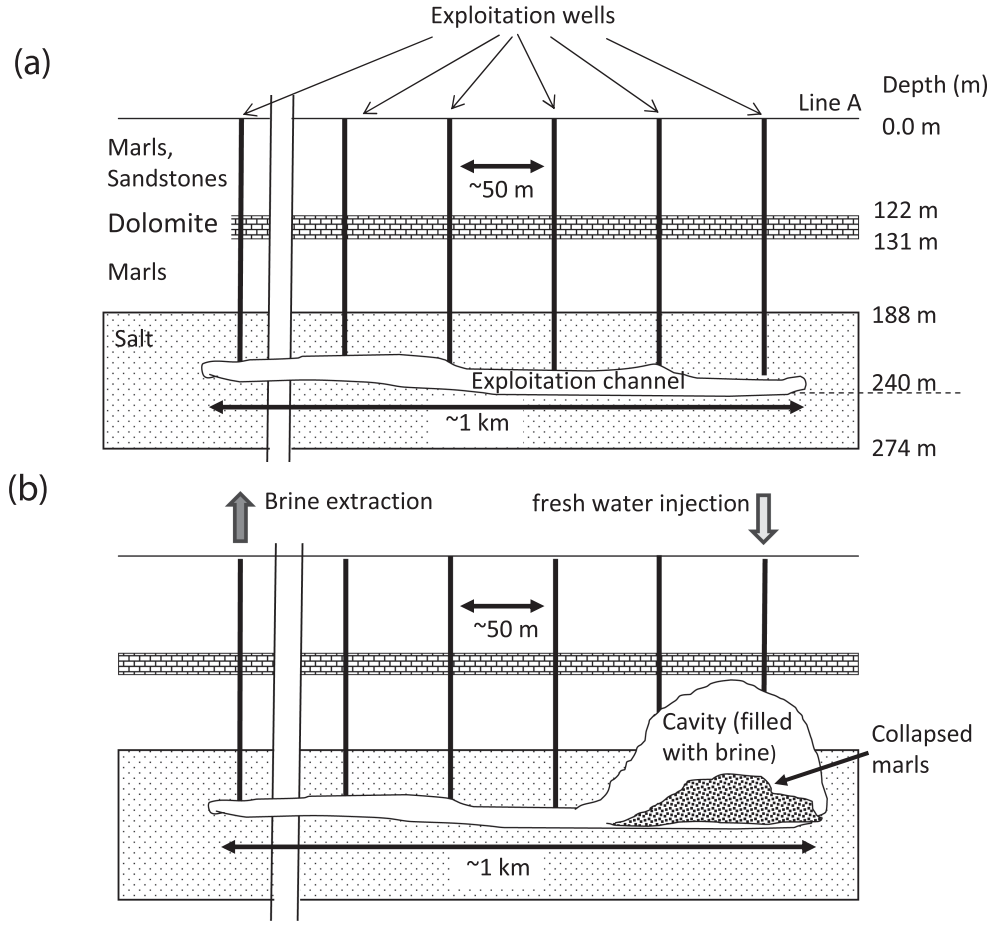

Figure 1. Schematic representation of two stages of the cavern mining. (a) Creation of the ∼1-km long and several metres thick exploitation channel through dissolution of the rock salt using water injection via the aligned exploitation wells. (b) Creation of the cavern through fresh water injection at the southern tip of the exploitation channel and brine extraction at the northern tip of the channel.

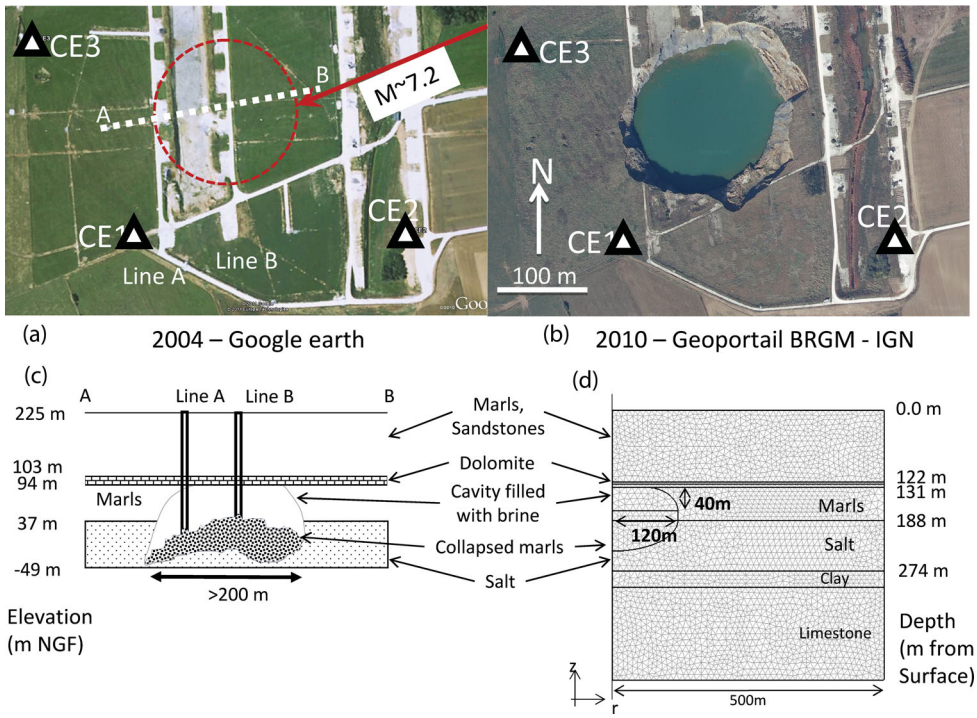

Figure 2. (a) Areal view (Google Earth) of the Cerville-Buissoncourt site in 2004, with the broad-band stations CE1, CE2 and CE3 (triangles), the exploitation wells (white rectangles) along two parallel N–S lines A and B, the cavern limits at the beginning of the experiment (thin dashed red line). The thick white dash line A-B corresponds to the section shown in Fig. 2(c). The red arrow indicates the propagation direction of the waves from the $M \sim 7.2$ earthquake that hit the cavern. (b) Same view as in Fig. 1(a), after the collapse on 2009 February 13. The white arrow indicates North direction. (c) Schematic cross-section of the salt cavern with 2009 dimensions before the collapse and a simplified geological structure with main lithological units (Table 2 for details). (d) Mesh of the finite element model with geometric dimensions of the geological units used (Table 2).

Table 2. Physical properties of each layer.[a]

Layer	Density (kg m^{-3})	Young's modulus (GPa)	Poisson's ratio (−)
Overburden	2500	10	0.25
Anhydrite	2910	79	0.29
Dolomite	2890	88	0.27
Intercalated marls	2657	15	0.30
Salt	2150	30	0.28
Collapsed rocks	2000	15	0.20
Clay	2500	12	0.25
Limestone	2500	21	0.25

[a]Based on: Mercerat (2007). Sismicité induite et modélisation numérique de l'endommagement dans un contexte salin. Thèse de doctorat LAEGO/INERIS et IPG Paris. Nothnagel (2003). Modélisation des instabilités en Mécanique des Roches : application à l'exploitation de la concession de Drouville. Thèse de Doctorat, École des Mines de Paris.

200 m NGF (Nivellement General de la France; i.e. ∼2.32 MPa, assuming a constant brine density of ∼1200 kg m^{-3} at 25°C) to 165 m NGF (∼1.91 MPa) at ∼15:30 UTC, followed by a constant pressure phase for about 13 hr. On 2009 February 11, pressure was lowered again at 04:20 UTC down to 145 m NGF (∼1.68 MPa) at 17:50 UTC. At that time, although pumping was stopped for an hour, we observed a sharp rise of the brine level, a strong change in the subsidence regime recorded by deformation instruments (Daupley *et al.* 2010) and a sharp increase in the rate of local seismicity activity (Fig. 3). These changes are interpreted by the start of the irreversible overburden collapse due to the rupture of the Dolomite, which led to the surface collapse on February 13 at 4:45 UTC.

2.2 Broad-band seismicity observations during the 3-days collapse events

At Cerville-Buissoncourt, the use of broad-band seismometer was mainly motivated by the idea that different types of earthquakes may well happen. Broad-band records include not only high frequency (5–50 Hz) signals associated with local microseismic activity due to the damage of the brittle rocks surrounding the cavern, but also low frequency (0.017–5 Hz) signals associated with long-period phenomena during the collapse (Jousset *et al.* 2010) and long-periods waves associated with remote large tectonic earthquakes.

Seismic signals observed on volcanoes and hydrothermal systems are classified according to their frequency content (e.g. McNutt 2000). In our broad-band seismological data, we observed three types of earthquakes, which we may classify according to their frequency content, although the contexts are not really the same. At Cerville-Buissoncourt:

(1) We define microearthquakes the signals containing frequencies ranging 2–50 Hz (Fig. 4, top). It is widely accepted that they correspond to brittle fractures of stressed rocks.

(2) We define 'long-period' (denoted LP) earthquakes the signals containing frequencies ranging 0.2–5 Hz (Fig. 4, bottom). On hydrothermal systems and volcanoes, suggested mechanisms for LP earthquakes include resonance of fluid-filled cavities (Chouet 1986; Ferrazzini & Aki 1987; Jousset *et al.* 2003, 2004) or oscillations due to fluid-driven flow (Julian 1994). Frequencies are the same at all stations of the network (two stations are shown), which demonstrates that the mechanism, which produces those frequencies is a source process and not a path effect. The presence of brine circulating in cracks within the collapsing cylindrical overburden may be one mechanism for such signals.

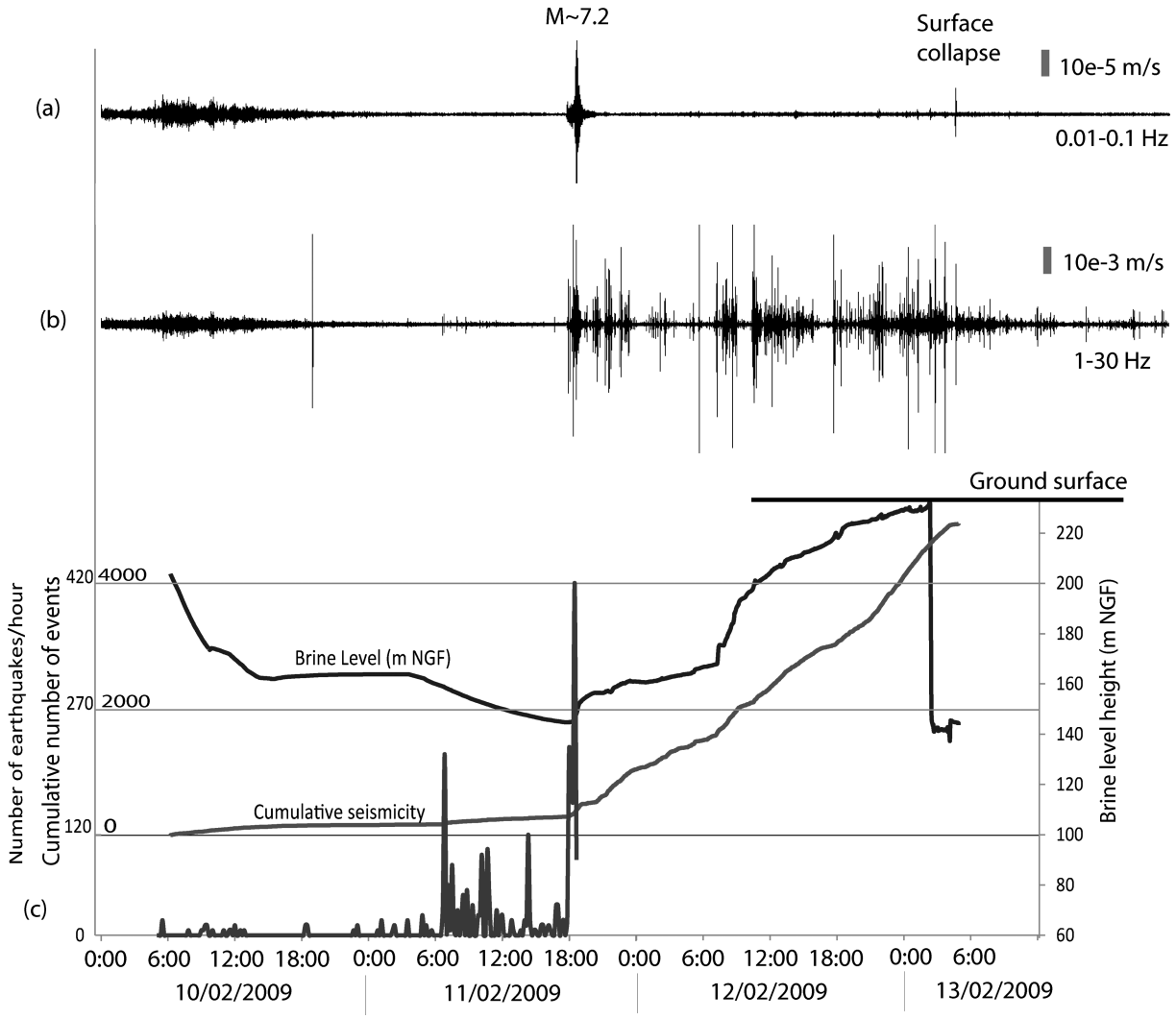

Figure 3. (a) Seismic record (station CE1) low-pass filtered (0.01–0.1 Hz) showing long period waves from the $M \sim 7.2$ Kepulauan Talaud, Indonesia earthquake. The high amplitude event on February 13 at 4:45 UTC is the surface collapse (see Fig. 4 for details). (b) Same seismic record as in Fig. 2(a) high-pass filtered (1–30 Hz) revealing microseismic earthquakes associated to the local collapse. High frequency noise on 2010 February 10 from ∼06:00 UTC to ∼18:00 UTC is due to a snow storm. (c) Number of microearthquakes recorded by the broad-band network correlated with the brine level temporal evolution (measured at 1 km from the cavern) between 2009 February 10 and 13. The sudden decrease of the brine level on 2010 February 13 at ∼02:00 UTC is due to instrumental artefact because brine over-flooded out of the well at surface.

(3) Very-long Period (VLP) earthquake have frequencies lower than 0.2 Hz. They are linked to inertial displacement of material (e.g. Chouet *et al.* 2005; Jolly *et al.* 2012). At the final collapse, the broad-band stations recorded a large amplitude VLP signal (Jousset *et al.* 2010) clearly associated with the surface collapse (See photo of the lake after cavern collapse, right top panel, Fig. 2 and the seismic signal and its spectrum in Fig. 5).

Fig. 5(a) shows details of the signals recorded during the surface collapse. The spectral content of the collapse signal is very rich (Fig. 5b), reflecting many mechanisms, including brittle fracture within the collapsing blocks, brine flow from the cavern to the surface and inertial movements of the large blocks of the overburden falling down into the cavern. We note a dominant period around 10–15 s. This period corresponds to oscillations starting just at the time of the final collapse lasting several minutes (signal not shown in Fig. 5). This observation suggests that a resonance mechanism takes place after the surface collapse and was triggered by the collapse itself. Oscillating inertial waves ('seiche') within the newly formed lake (Jackson 1833) after the collapse may be invoked. A fundamental frequency of 12 s requires a depth for the newly formed lake about 50–100 m (with a diameter of 200 m, see Fig. 2), which is the order of magnitude of the cavern's height before its collapse. We discuss the significance of this peak further later in the paper as a possible natural resonance frequency of the cavern + conduit system.

2.3 Dolomite rupture and teleseismic remote waves

The number of microseismic events is strongly correlated with the phasing of the brine pumping operations resulting in pressure lowering (Fig. 3). From few microearthquakes per day prior to the starting of the pumping operations, the number of earthquakes slightly increased to less than 10 earthquakes per hour in the 3 hr preceding the Dolomite rupture. The local microseismic events rate increased to more than 200 earthquakes per hour on February 11 at 17:50

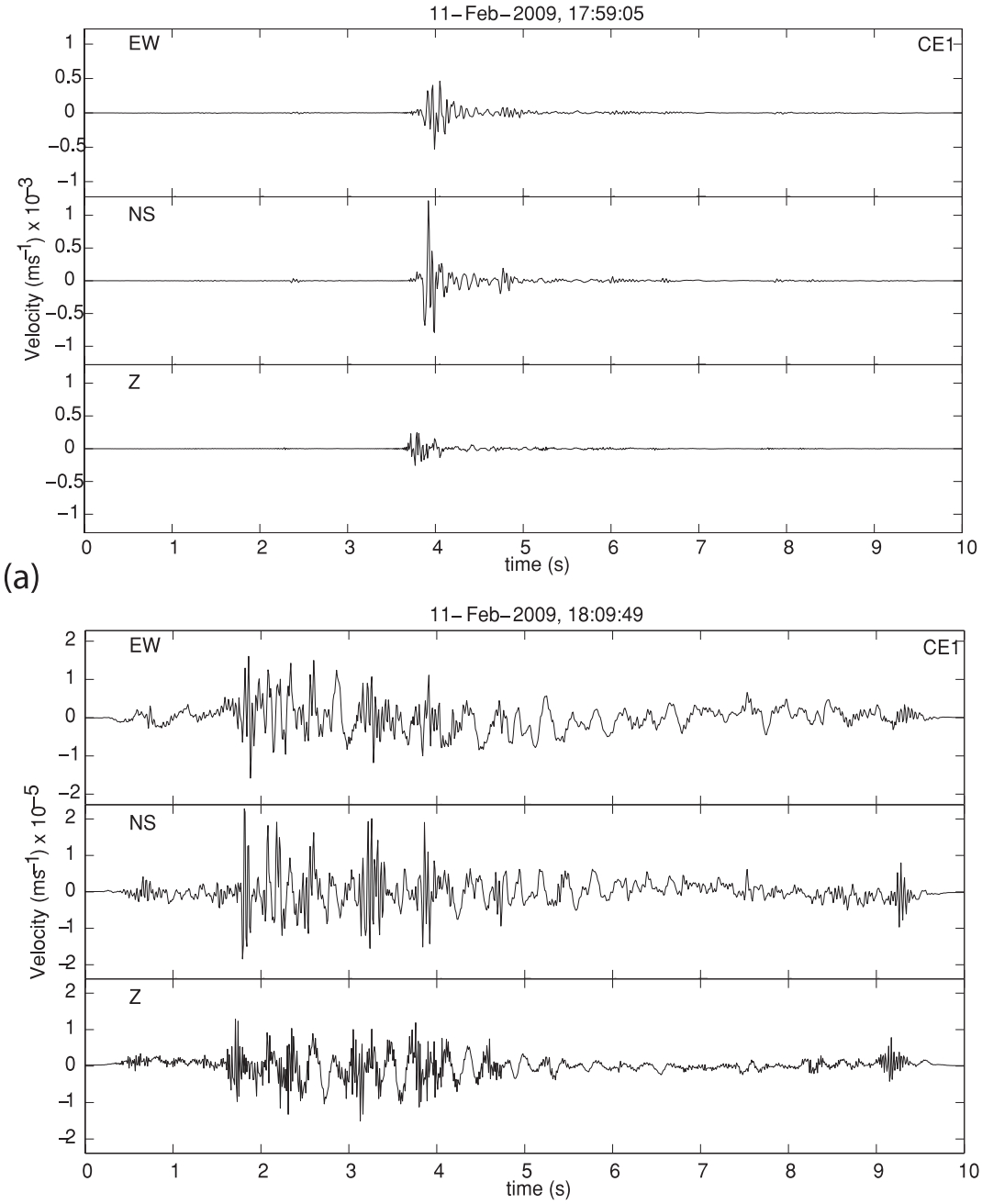

Figure 4. (a) Three-component records of the ground velocity records at station CE1 for two types of earthquakes; (top panel) microearthquake associated with brittle rupture; (bottom panel) long-period earthquake overprinted with small microearthquake. (b) Corresponding spectra of the signals shown in Fig 3a. Note the similar frequency content in the long-period earthquake seen at two different stations (spectrum at CE3 is also shown).

UTC for more than 40 min. The number of earthquakes decreased to down to about 50–70 microearthquakes per hour 2 hr later. It remained at about the same level up to the surface collapse. In total, more than 5000 microearthquakes were recorded on the broad-band stations.

Surprisingly, the dramatic increase in local seismicity rate occurs within seconds of the arrival of body and surface waves generated by an $M \sim 7.2$ earthquake at 17:34:50 UTC at Kepulauan Talaud (Indonesia, latitude $\sim 3.902^{\circ}$, longitude $\sim 126.4^{\circ}$, depth 20 km), that is, $\sim$11 800 km distant from the cavern (Figs 3 and 6).

Careful analysis of the occurrence times of the microearthquakes with respect to the remote waves reveals that the most powerful microearthquakes (based on amplitudes) occurred when surface waves passed on the cavern (Fig. 6); in addition, at several occasions body wave's phases were also accompanied with single larger microearthquake. The first large microearthquake is in phase with the *SKiKP* phase (at 17:56:46 UTC); the following largest microearthquakes happen after the phases PS passed (18:02:45 UTC) and at the time of the *PKKP* sequence (18:04:30–18:04:50 UTC). Then, several small earthquakes

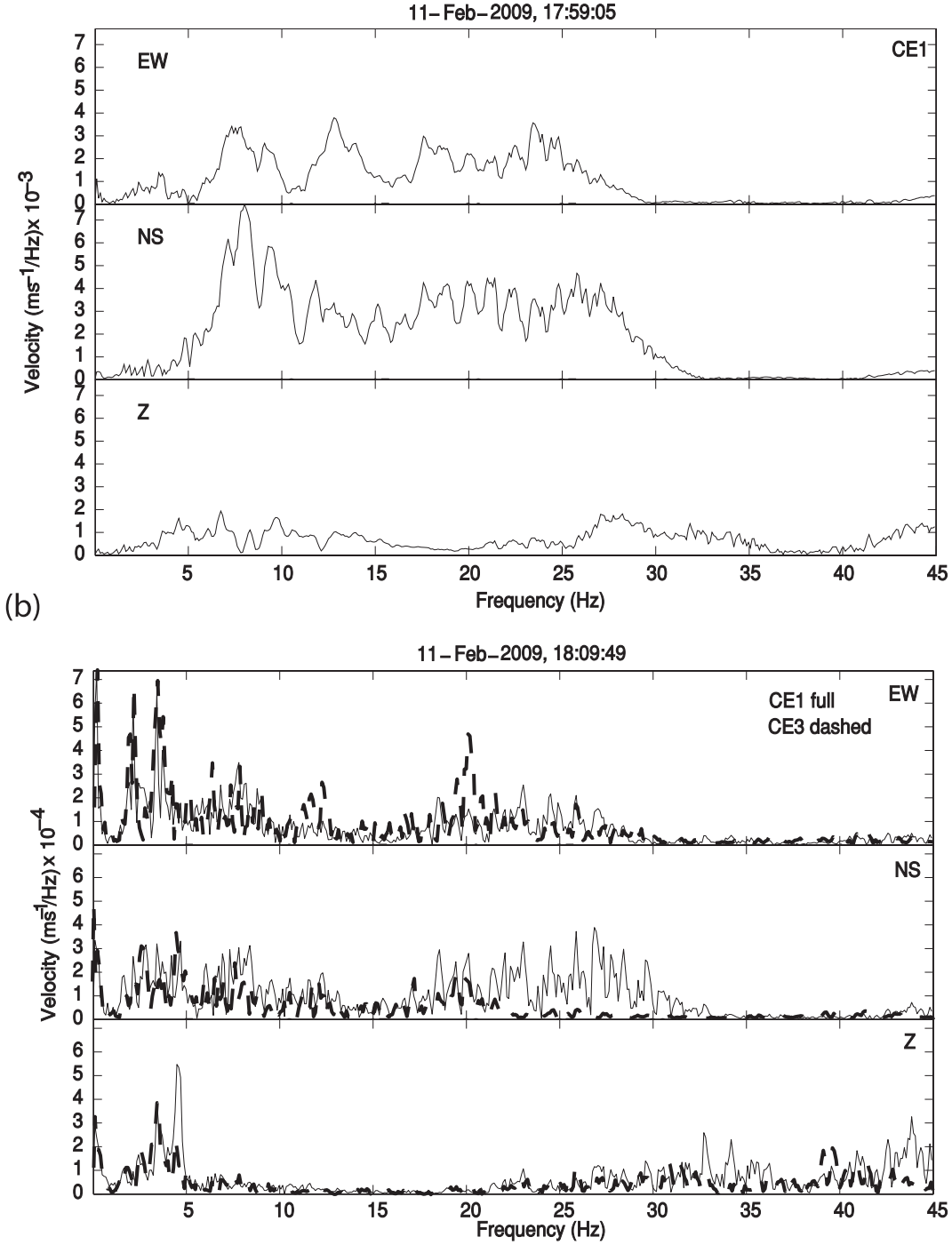

Figure 4. (*Continued*.)

occurred during the *SKKP* and *SKKS* phases with a swarm of larger microearthquakes (18:09:30–18:10:00 UTC). Another high frequency microearthquakes swarm occurred at 18:18 UTC, with no apparent correlation with expected arrival of waves (Lay & Wallace 1995) from the Kepulauan Talaud earthquake. The dramatic rate increase occurred at 18:24:30 UTC, and coincides with the beginning of the Rayleigh waves train (Fig. 6). The relative microearthquake magnitudes (based on the amplitudes) were much higher when the seismicity rate was higher. The correspondence between the amplitude peaks of the surface waves and the occurrence of microearthquakes is sometimes striking (Fig. 6b). Note that once the surface waves train had passed, both microseismicity rate and amplitudes decreased (Figs 3 and 9).

These observations suggest the triggering of the local seismicity by stress changes due to remote long period seismic waves. Therefore, we naturally question the possible mechanism for the causal relationship between the passage of the earthquake and the sudden increase of the local seismicity activity, that is, the possible remotely

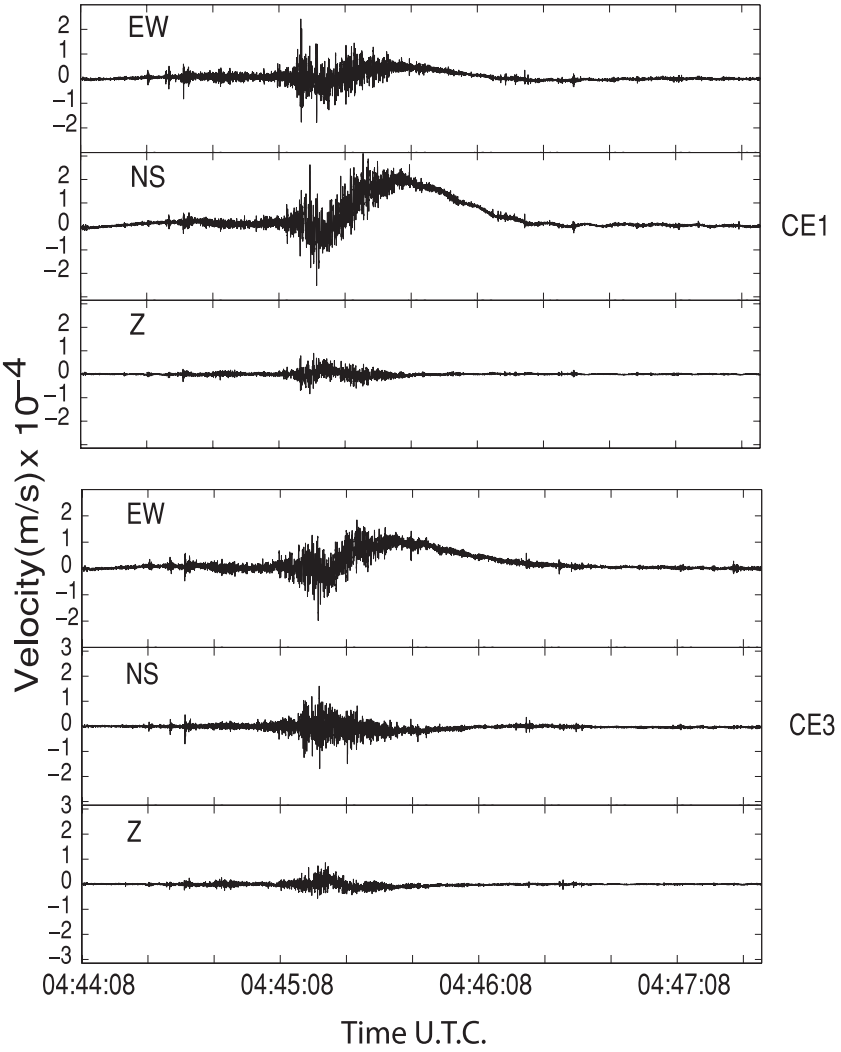

Figure 5. (a) Three component record of the ground velocity record at station CE1 at the time of the surface collapse. (b) Corresponding spectra revealing the strong very-long-period component of the collapse and low frequency content in the signals. Note the peak at ∼0.1 Hz (especially visible on the NS component of both stations), which corresponds to the resonance of the collapsed cavern just after the surface collapse, suggesting a natural frequency of the cavern + brine + overburden system at long periods (10–20 s).

triggered increase of overburden damage, and possibly acceleration of the collapse.

3 CRITERIA FOR REMOTE TRIGGERING

3.1 Previous observations

Stress changes induced by earthquakes are categorized as (1) permanent, that is, static and (2) transient, that is, dynamic associated with the passage of seismic waves (Manga *et al.* 2009). The amplitude of static stress decays as power-law function of the distance from the epicentre with exponent −3, whereas dynamic stresses propagating with seismic waves decays more slowly as a power-law function of the distance with exponent ∼−1.5 and −2 for surface and body waves, respectively (Hill & Prejean 2007), the former type of waves inducing the largest amplitude shaking (Brodsky & Prejean 2005). As suggested by various authors (Gomberg *et al.* 2001; Manga & Brodsky 2006; Hill & Prejean 2007), only dynamic stresses are significant in the far field.

Several studies (Peng *et al.* 2009; Rubinstein *et al.* 2009; Cannata *et al.* 2010) outlined that one major controlling factor in the remote triggering potential of a teleseismic earthquake is the peak dynamic stress magnitude of the order of a few to tens of kilopascals. For instance, Cannata *et al.* (2010) reported a peak dynamic stress of 13 ± 3 kPa and 4 ± 0.7 kPa at Etna volcano (Italy) for an $M \sim 6.8$ Southern Greece earthquake in 2006 (760 km distant) and the $M \sim 7.9$, Sichuan province (China) earthquake in 2008 (7830 km distant), respectively. Even smaller threshold values have been reported, that is, 7–8 kPa threshold recently inferred by Chao *et al.* (2011) at Taiwan based on 45 teleseismic earthquakes, or 2.4 kPa threshold estimated for the 2007 M_w 8.1 Solomon event, or tremor-triggering with ∼2–3 kPa threshold at Parkfield in central California (Peng *et al.* 2009), or long-range triggering down to ∼0.1 kPa in some instances (van der Elst & Brodsky 2010).

3.2 Dynamic strain and stress computation

After instrumental responses have been removed from our broadband records, peak particle velocity of the surface waves (dominant

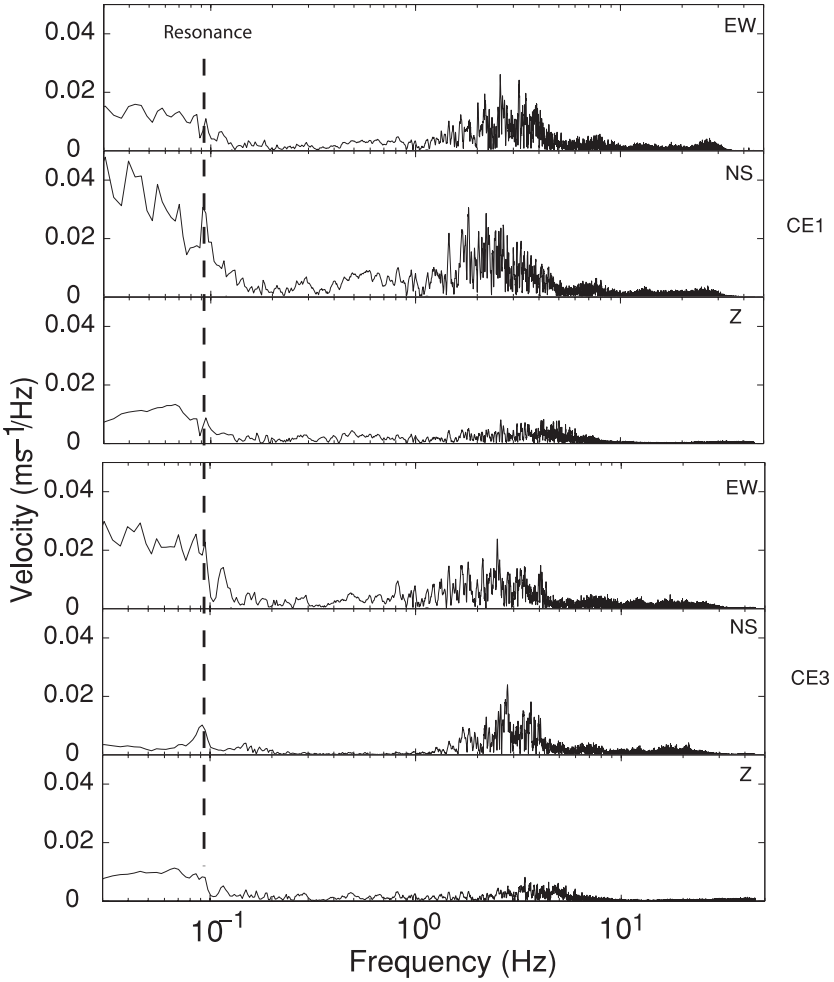

Figure 5. (*Continued*.)

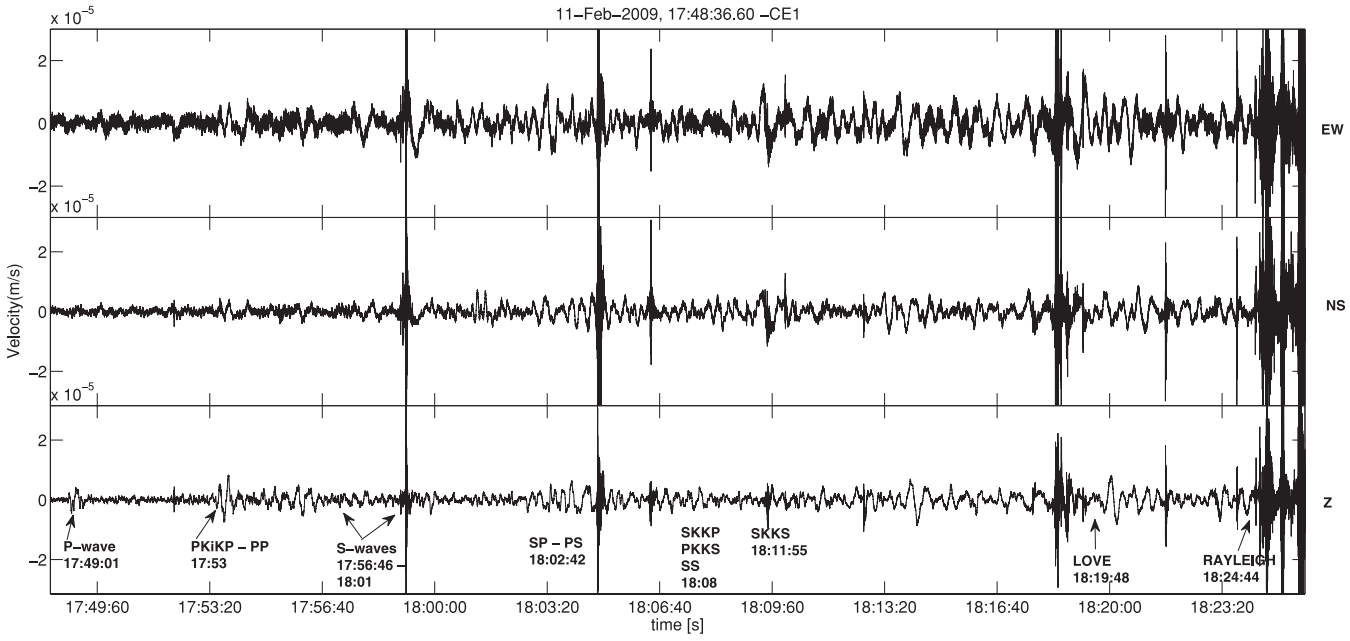

Figure 6. Details of time correlation between stress changes due to remote teleseismic long-period waves recorded at station CE1 associated to local microearthquakes (a) Body wave correspondence. (b) Detail of the surface wave correspondence; longitudinal and transverse signals (see text for details).

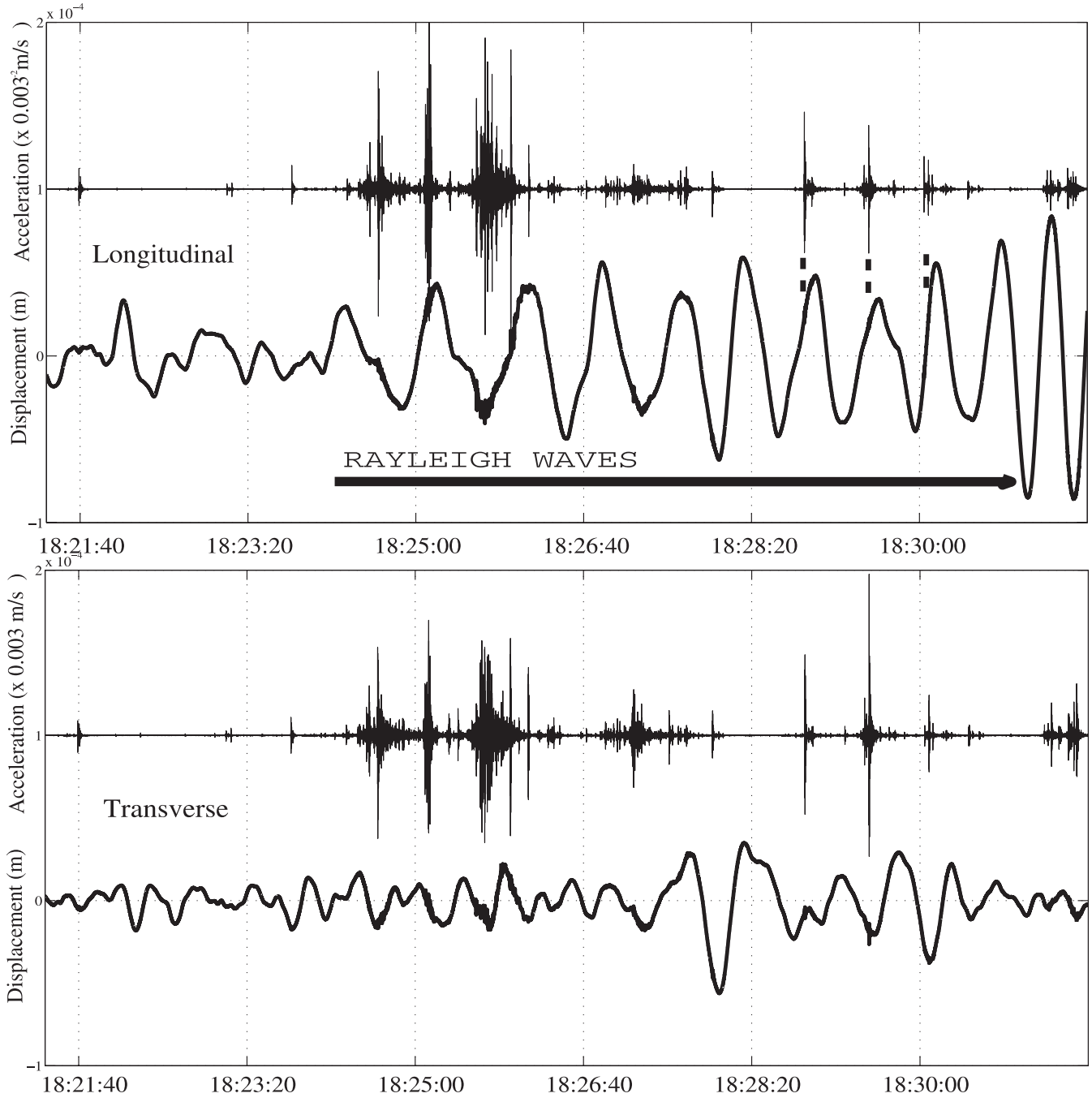

Figure 6. (*Continued*.)

frequency of 0.03–0.1 Hz) reach ∼4.5 10^{-5} m s^{-1}. We note that this small value is almost twice as high as the expected amplitude value (Lay & Wallace 1995); this may be explained by the presence of the cavern (Nasseri-Moghaddam *et al.* 2007) which traps and concentrates seismic energy, increasing the amplitude of the ground response above and around the cavern (Smerzini *et al.* 2009). The increased dynamic stress could therefore contribute to amplify possible triggering mechanisms of local microseismicity around the cavern, even if of low amplitude. In order to estimate the dynamic stress generated by the surface waves on the cavern, we used two methods.

In the first method, we investigate stress at the cavern depth from our surface observations. We extrapolated the observed dilatational strains to depth using solutions for Rayleigh wave equation for a simple half-space structure (e.g. Lay & Wallace 1995), and we calculate the displacements and then the resulting strain and stress components. Miyazawa & Brosdky (2008) showed that the normal strain changes across radial e_{rr} and vertical e_{zz} directions and the shear strain changes e_{rz} at depth can be obtained by

$$e_{rr} = \frac{e^{\mathrm{ref}}_{rr}}{u_{z(z=0)}} u^{\mathrm{obs}}_{z}$$
$$e_{zz} = \frac{e^{\mathrm{ref}}_{zz}}{u_{z(z=0)}} u^{\mathrm{obs}}_{z}$$
$$e_{rz} = e_{zr} = \frac{1}{2}\left(\frac{u_{r,z}}{u_{r(z=0)}} + \frac{u_{z,r}}{u_{r(z=0)}}\right) u^{\mathrm{obs}}_{r} \quad (1)$$

with

$$e_{rr}^{\mathrm{ref}} = -A_0 k^2 \cos(kr-\omega t)\left[\exp(-\omega\eta_\alpha d) + \frac{1}{2}\left(\frac{c^2}{\beta^2}-2\right) \times \exp(-\omega\eta_\beta d)\right]$$

$$e_{zz}^{\mathrm{ref}} = A_0 k\ \cos(kr-\omega t)\left[c\omega\eta_\alpha^2 \exp(-\omega\eta_\alpha d) + \frac{\omega}{2\mathrm{c}}\left(\frac{c^2}{\beta^2}-2\right) \times \exp(-\omega\eta_\beta d)\right]$$

$$\frac{u_{r,z}}{u_{r(z=0)}} = 2\frac{\beta^2}{c^2}\left[\omega\eta_\alpha \exp(-\omega\eta_\alpha d) + \frac{\omega\eta_\beta}{2}\left(\frac{c^2}{\beta^2}-2\right)\exp(-\omega\eta_\beta d)\right]$$

$$\frac{u_{z,r}}{u_{r(z=0)}} = 2\mathrm{k}\frac{\beta^2}{c^2}\left[c\eta_\alpha \exp(-\omega\eta_\alpha d) + \frac{1}{2\mathrm{c}\eta_\beta}\left(\frac{c^2}{\beta^2}-2\right)\exp(-\omega\eta_\beta d)\right]$$

$$u_{z(z=0)} = A_0 k\ \cos(kr-\omega t)\left[c\eta_\alpha + \frac{1}{2\mathrm{c}\eta_\beta}\left(\frac{c^2}{\beta^2}-2\right)\right], \qquad (2)$$

where A_0 is a constant, k is the wave number, ω is the angular frequency, r is the radial distance, d is the depth, t is the time, α is the compressional wave velocity, β is the shear wave velocity and c is the phase velocity of the Rayleigh wave, u_z^{obs} and u_r^{obs} are the observed vertical and radial (in the direction of the Rayleigh wave propagation) components of the displacement at surface, $u_{z(z=0)}$ is the observed vertical particle motion at surface, and

$$\eta_\alpha = \sqrt{\frac{1}{c^2}-\frac{1}{\alpha^2}},\ \eta_\beta = \sqrt{\frac{1}{c^2}-\frac{1}{\beta^2}}. \qquad (3)$$

The Rayleigh-wave dynamic stress tensor with compression taken as positive is

$$\delta T_R = -[\kappa\delta\Theta(t)\mathrm{I} + 2\mathrm{G}\delta\mathrm{D}(t)], \qquad (4)$$

where κ and G are the bulk and shear elastic modulii, respectively; $\delta\Theta(t) = e_{ii}(t)$ is the dynamic dilatational strain; I is the identity matrix; and

$$\delta D(t) = \delta E(t) - \frac{1}{3}\delta\Theta(t)\mathrm{I}$$
$$\delta E(t) = [e_{ij}(t)] \qquad (5)$$

Similar formulas can be derived for Love waves (Hill 2010). This approach leads to dynamic stresses ranging 1–2 kPa.

In the second method, we took the opportunity to have close stations (distance of about 250 m) in order to estimate the strain only from our records. We integrated the three-component velocity records into displacement records at each station. Knowing the relative positions of the stations (Fig. 2) and elastic properties (Table 1), we computed the dynamic strain and stress tensors with time. By analysing stresses for different waves in our record, we obtain peak dynamic stress values in the range 0.1–2 kPa. For instance, *P*-wave corresponds to a peak-to-peak dynamic stress of the order of 0.4 ± 0.2 kPa. The *S*-wave corresponds to a peak-to-peak dynamic stress reaching 1 ± 0.5 kPa. Both Love and Rayleigh waves correspond to peak-to-peak dynamic stresses up to 2 kPa.

Stresses are dependent on the layer where the stress is computed and may be influenced by the regional stress. The Cerville-Buissoncourt sedimentary deposits comprise marls sandstones and the Dolomite layer (Fig. 2; Table 2). Higher dynamic stresses are obtained in the large rigidity Dolomite layer. The regional stress in the area is poorly known, and we assume it to be isotropic (Nothnagel 2003; Mercerat 2007).

3.3 Near critical state of the fluid-filled cavern

To be sensitive to such small dynamic stresses, the system comprising the low pressurised brine cavern, the highly stressed Dolomite layer should be in near critical state, that is, close to or undergoing failure, before the arrival of the waves (Di Grazia *et al.* 2009; Rubinstein *et al.* 2009; Gomberg 2010; Hill 2010; Cannata *et al.* 2010).

Several observations at the Cerville-Buissoncourt site before the 2009 collapse have shown the susceptibility of the system 'brine-filled cavern + Beaumont dolomite + overburden' to change in response to very small stress perturbations (Mercerat *et al.* 2010). The evolution of vertical displacements recorded at extensometers located at the Dolomite layer depth was monitored during two pressure tests conducted in 2005 and 2007. They consisted in a short brine pressure lowering (of 40 and 20 kPa, respectively) followed by a pressure restoration to its initial value. Negligible recovery in the strain-metre data in the pressure restoration phase indicated an irreversible behaviour of the cavern overburden and a very likely damaged state of the intercalated marls composing the overburden (Mercerat *et al.* 2010). During the pumping operations in 2009 aiming at the cavern collapse, the brine pressure was lowered by a much larger value (more than 70 kPa); therefore, small stresses variation could be sufficient to trigger the collapse. The cavern was therefore about to collapse when the long-period remote waves hit it.

In order to quantify the near critical state of the system prior to the collapse, we modelled the pressure changes of inner cavern pressure induced by pumping operations using 2-D axisymmetric elastic finite-element simulations of the cavern (see mesh in Fig. 2d). The cavern dimensions are monitored directly with *in situ* (courtesy of the exploiting company), but due to the risk of sudden collapsing associated to a late survey, the exact cavern geometry was not known in 2009. We assumed its geometry (radius of about 100–120 m and height of about 40 m, see Fig. 2) from the last sonar survey in 2004 and the location of earthquakes seismicity (Daupley, private communication 2011). The top of the cavern is located at ∼130 m depth (below the Beaumont dolomite layer). Assuming an *in situ* initial stress state isotropic and equal to the lithostatic vertical stress, the spatio-temporal evolution of stress state during the pumping phasing of 2009 is calculated so that both excavations of the cavern and changes of inner cavern pressure were modelled by modifying the nodal forces applied at the cavern walls.

Let us define the failure zone as the region where the Coulomb stresses σ_{coul} exceed zero. The Coulomb stresses σ_{coul} are formulated from the minimum and maximum principal stresses σ_{min} and σ_{max} obtained from the elastic calculations (King *et al.* 1994), and assuming that a cohesionless fluid-filled fracture could exist at any point of the studied zone

$$\sigma_{\mathrm{coul}} = 0.5\cdot(\sigma_{\mathrm{max}}-\sigma_{\mathrm{min}})\cdot(\sin(2\beta)-\mu\cos(2\beta)) - 0.5\cdot(\sigma_{\mathrm{max}}+\sigma_{\mathrm{min}}), \qquad (6)$$

where μ^* of average value 0.4 (e.g. King *et al.* 1994) is the effective friction coefficient accounting for the presence of fluid within the fracture and is expressed according to standard isotropic poroelastic relation $\mu(1-B)$ with μ the friction coefficient and B the Skempton's coefficient, typically ranging from 0.5 to 0.9 (e.g. Roeloffs 1996). The orientation angle of the cohesionless fracture β is assumed to be critically oriented accordingly to the stress directions so that $\beta = 0.5.\arctan(1/\mu^*)$. Fig. 7 depicts the evolution of the failure zone estimated for μ^* varying between 0.4 and 0.6 during the pumping phases. It shows that the zone of failure is very likely to cross the whole cavern overburden (the stiff Dolomite and marls), that is,

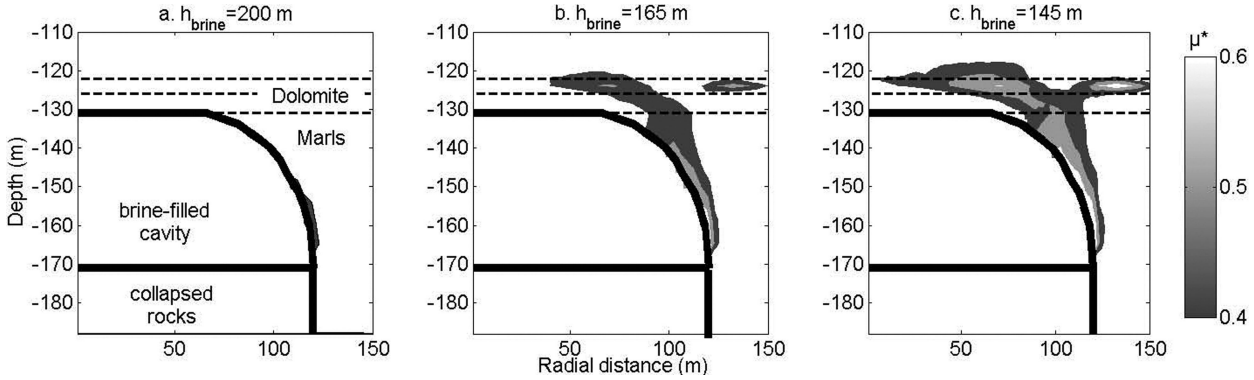

Figure 7. Evolution of the Coulomb stresses calculated for optimally oriented cohesion-less fractures assuming different effective friction coefficient μ^* (varying between 0.4 and 0.6) during the pumping phases (a: start of pumping with brine level $h_{\text{brine}} = 200$ m; b: constant pressure phase with $h_{\text{brine}} = 165$ m; c: lowest brine level phase with brine level $h_{\text{brine}} = 145$ m). The heavy black line defines the volumes of the brine-filled cavity and the underlying collapsed rocks.

creation of a macro-scale discontinuity, considering μ^* of $\sim$0.5. The influence of μ^* is further discussed later.

4 MECHANISMS FOR DYNAMIC TRIGGERING

4.1 Triggering mechanisms

Though the underlying physical mechanisms for dynamic triggering remain a matter of continuing research studies, two main mechanisms are usually invoked to explain remote triggering, either (1) fluid activation and transient deformation, for example, (Miyazawa & Brosdky 2008), and (2) frictional failure on critically stressed faults (Hill 2010). The first mechanism is generally characterized with a delay in the triggered seismic swarm occurrence with dominant energy release developing hours to days after the passage of the surface waves (Hill 2010) and recently observed at Mount Etna (Cannata *et al.* 2010) with a delay of 2 hr of the swarm occurrence after the passage of the earthquake waves. Careful look at the timing of the microearthquakes with respect to the long period waves indicates that most large microearthquakes occur at the time or shortly after the Rayleigh waves hit the cavern (Fig. 6a), with a more significant correspondence with the longitudinal signal (Fig. 6b). We suggest that the second mechanism is therefore more efficient than the first one in our case, as it is consistent with observed prompt onset of triggered seismicity (Hill 2010), although the presence of the brine may also contribute to a lesser extent or later in the collapse processes, and more specifically in the resonance of the system as discussed later.

4.2 High sensitivity of the system

We assume that the surface-wave dynamic stresses induce a triggered response, which corresponds to an initiation of fracture slip by temporarily boosting the total stresses acting on the preexisting fracture planes toward the failure threshold. We approximate the failure threshold by a combination of Coulomb failure for dynamic shear stresses and by Griffith mixed-mode failure for dynamic dilatational stresses (Hill 2010). Failure once initiated will be controlled by dynamic friction, rate-state friction, or crack-growth dynamics (Noda *et al.* 2009). Let us define the increment of stress δT as the additional stress magnitude necessary to initiate the whole rupture of the Beaumont dolomite layer (creation of a macroscale discontinuity across the formation), so that $\sigma_{\text{coul}} + \delta T$ exceeds zero over the whole thickness of the Beaumont dolomite layer.

Fig. 8 depicts δT assuming $\mu^* = 0.495$; 0.497 and 0.5 (Figs 8a–c, respectively) and shows that δT varies from a few kilopascals to tens of kilopascals. Focusing on the point 1 where δT is minimum, the parametric analysis (Fig. 6d) demonstrates the very high sensitivity of δT to μ^* such that it ranges from $\sim$2 to $\sim$20 kPa when varying μ^* by an increment of only 0.005 (1% of the nominal value of 0.5), corresponding to a change of less than 1° in terms of effective internal friction angle.

Aside the uncertainties on both the cavern geometry and *in situ* conditions (e.g. rock properties, initial stress, and fractured state), several physical processes are not fully appreciated and deserve further investigations: ductility of the marls constituting the cavern surroundings that may have played a role in the 2005 and 2007 pressure tests (see above); strength and modulus degradation due to damage localization and accumulation over the loading whole history of the system from 2004 to 2009 (see e.g. Amitrano 2006); fluid-mechanical interaction such as liquefaction as invoked to explain failure of fault gouge (Gomberg *et al.* 2001) and possibly the softening-to-weakening dynamic non-linear behaviour of the fractured (quasi granular) medium surrounding the cavern (see experimental studies at lab scale by Johnson & Jia 2005). Hence, care should taken not to consider the calculated δT of 2–20 kPa as a direct comparison measure, but rather as evidence of the unstable state reached by the system at the final stage of pumping and during the passage of teleseismic surface waves.

A complementary approach to the afore-described physical-based method would focus on the investigation of the statistical significance of the suspected dynamic triggering. Over the last decades, several statistical tests have been developed (see a review by Marsan & Nalbant 2005), either using modified versions of the commonly used β-statistic (see Gomberg *et al.* 2001 and Hough 2005), or using new statistic, as the one recently developed by van der Elst & Brodsky (2010) based on the interevent times. The basis of all these statistical tests is the estimate of the probability of the observed increase on the number of earthquakes (see Fig. 3) occurring by chance using an estimate of the background seismic rate, that is, analysing a local earthquake catalogue over the study period. Yet, this approach in the case of Cerville-Buissoncourt would require analysing the events when the system has reached its critical state, that is, over a very short time interval (less than a few days or even hours), hence greatly limiting the number of events in the catalogue and its completeness.

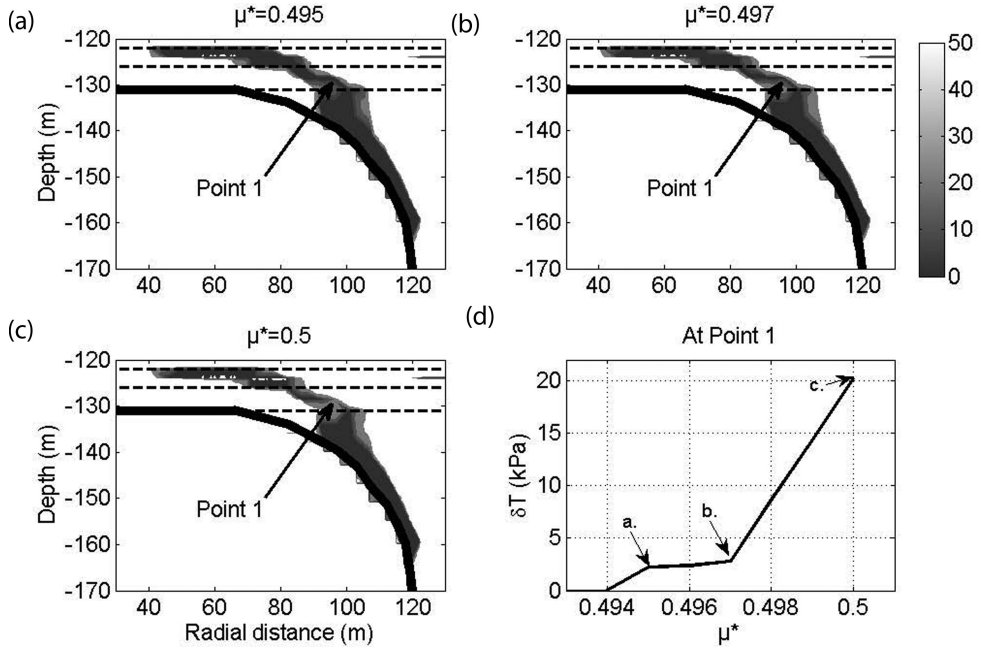

Figure 8. (a), (b), (c): Iso-contour of the increment of stress magnitude δT (expressed in kPa) necessary for the failure zone to cross the entire thickness of the dolomite layer. The failure zone is defined as the region where the Coulomb stresses exceed zero, respectively assuming $\mu^* = 0.495$; $\mu^* = 0.497$ and $\mu^* = 0.5$. The point 1 indicates the location where δT and μ^* were sampled, as shown in (d): relationship between δT and μ^* at the point 1; the values δT corresponding to each cases (a, b, c) are reported.

Therefore, we restrict our analysis to the inspection of the large earthquake (magnitude larger than 7) catalogue in the year preceding the collapse. This analysis did not reveal any change of the seismicity rate when surface waves passed at the cavern site. This confirms that seismicity triggering under normal conditions does not occur and that triggered seismicity requires the system to be in a critical state.

4.3 Role of frequency

The cavern rupture initiation may not be only explained by the magnitude of the stress perturbation. As outlined by several authors (Brodsky & Prejean 2005; Peng *et al.* 2009; Rubinstein *et al.* 2009; Guilhem *et al.* 2010; Chao *et al.* 2012), the transient nature of the teleseismic waves, and the frequency content of the signals, may also play a role.

In particular, one commonly invoked mechanism for microearthquake triggering is oscillatory stress changes due to Earth tides (e.g. Cochran *et al.* 2004; Metivier *et al.* 2009; Hawthorne & Rubin 2010). The amplitude of the stress is about 1 kPa for the M_2 phase, that is, of the same order as the one recorded during the passage of the surface waves at Cerville-Buissoncourt, but of very long period of ∼12 hr, that is, far larger than the 30 s period suggested by several authors. For instance, Brodsky & Prejean (2005) have suggested that long-period waves with dominant periods of about 30 s are more effective at generating local seismicity than short period waves of comparable amplitude. Yet, the role of Earth tides in modulating the earthquake rate accurately would be very challenging to investigate due to the short duration of the experiment at Cerville Buissoncourt.

A possible triggering process linked with a well-defined range of frequencies was also suggested at laboratory scale. Experiments either on nanoscale contacts (Socoliuc *et al.* 2006) or at larger scale, on sheared granular media (Johnson & Jia 2005) showed that small mechanical vibrations may help in driving a contacting sliding interface out of equilibrium when applied at suitable frequency and amplitude ranges. More recently Capozza *et al.* (2009) showed the appearance of a friction suppression regime in a well-defined range of frequencies that depends among others on the wave amplitude and on the loading. Furthermore, cyclic fatigue from the oscillatory waves may also be invoked as proposed by Gomberg *et al.* (2001).

Fig. 9 shows the relations of the observed microseismicity and filtered signals of the longitudinal and transverse long-period records. We show that the frequency content >0.1 Hz has no influence on the triggering of the high-frequency events. Microearthquakes were generated during the whole period of longitudinal and transverse waves (Fig. 9). The occurrence of microearthquakes started as soon as longitudinal signals (Rayleigh waves) with periods around 30 s or above hit the cavern (see e.g. the temporal correlation of the swarm of high-frequency events occurring around 18:24 in Figs 6 and 9). We acknowledge that the role of frequency may be more complex and a time-dependency effect may exist, as the frequency threshold for triggering appears not to be the same over the passage of waves. The swarm of high frequency events occurring before 18:36 (Fig. 9) may be correlated with the events within the range 0.033–0.05 Hz, but the swarm just after 18:36 (Fig. 9) may both be related to events within the range 0.033–0.05 Hz and 0.05–0.1 Hz.

We note that the excitation frequencies of the surface waves may be in the range of the natural frequency of the cavern system (dolomite, fluid-filled cavern and overburden). In Fig. 5(b), we observed a resonance frequency at ∼12 s; although the system is not the same before and after the collapse, we may interpret this value as being close to the natural frequency of the cavern system before its collapse.

As aforementioned, the exact cavern shape at Cerville-Buissoncourt was unknown in 2009 and instead of trying to model accurately the resonance natural frequency of the complex shape,

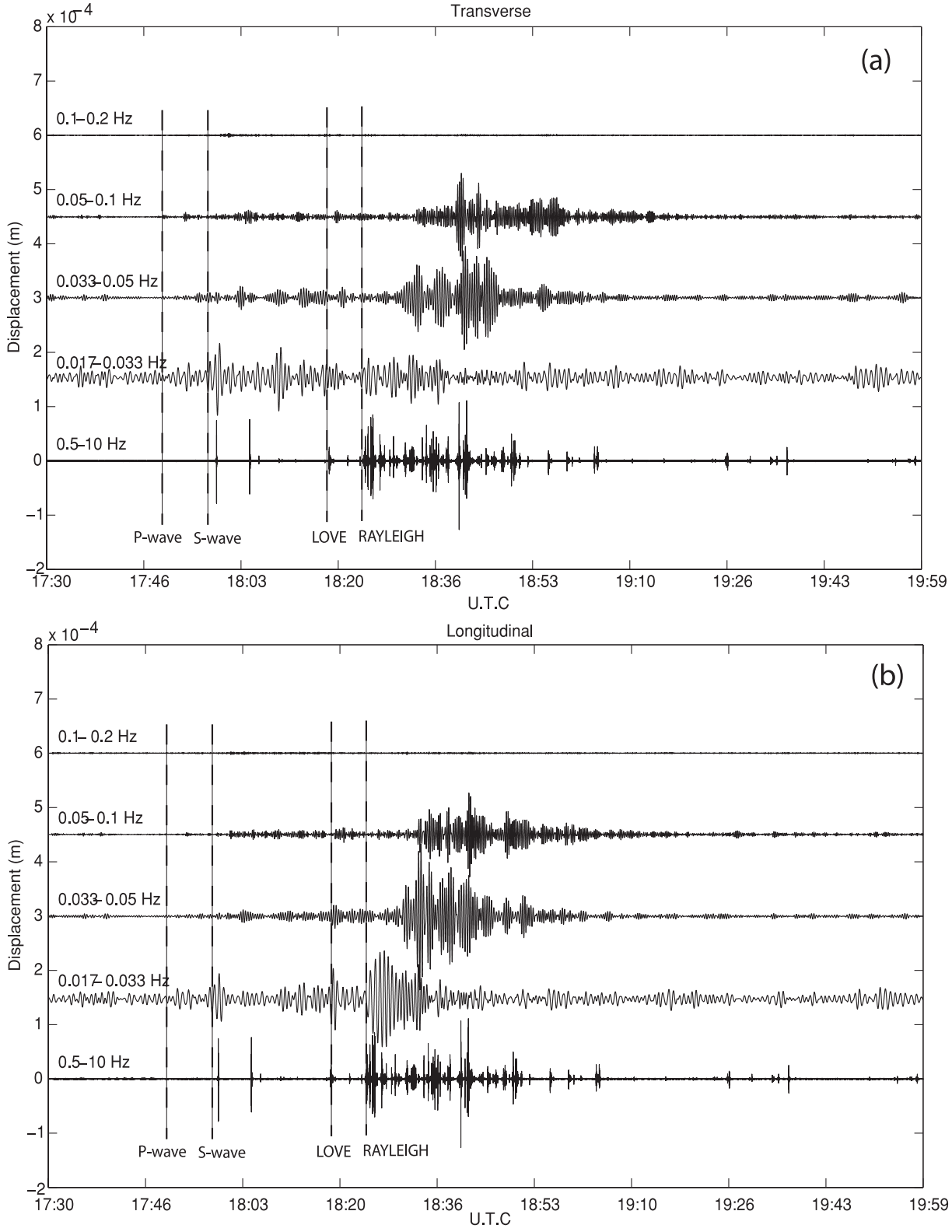

Figure 9. (a) Longitudinal (in the direction of the earthquake azimuth) and (b) transversal (in the direction perpendicular to the earthquake azimuth) of the seismic records station CE1 for different frequencies indicated at the upper left part of each trace. It appears that triggered seismicity started for Rayleigh waves at very long periods, and then that all periods (30 to 5 s) contributed.

we rather estimated it from simple approaches. Approximating the cavern system as a sphere (Kubotera 1974) does not satisfactorily explain our observations. For a cavern of radius r filled with a fluid having acoustic velocity α the underground cavern fundamental mode of vibration frequency f_0 may be approximated by

$$f_0 \approx \frac{4.4}{2\pi}\frac{\alpha}{r}. \quad (7)$$

Using eq. (7), a resonance fundamental period <20 s requires a cavern radius >20 km. The over-simplified geometrical vision of the cavern may overlook a major structural aspect corresponding to the fluid-filled channels (conduits) of several metres thick located behind the cavern in the salt layer (outlined by the white lines A and B in Figs 1 and 2). On this basis, we invoke a model of the resonance of the brine-filled NS exploitation conduit. Pressure waves initiated by the collapse travelled within the brine into the conduit. The impedance contrast between the brine and the surrounding rock traps the seismic energy into the conduit generating the resonance. Similar models have been invoked on volcanoes to explain the occurrence of long-period signals (Chouet 1986; Neuberg 2000). This type of models was studied in great detail, as they are able to explain many characteristics of long-period signals with reasonable resonator sizes (Ferrazzini & Aki 1987).

In order to find the natural frequencies of the system, we investigated the impulse response of the exploitation conduit modelled as a 1-km long, 5 to 10 m thick dyke filled with brine (density of 1100 kg/m^3; acoustic velocity of 1500 m/s). We modelled wave propagation in viscoelastic media with finite-difference methods, following the approach of Jousset *et al.* (2003) and Jolly *et al.* (2012). We numerically triggered a 10 s long source in the dyke at a defined location within the conduit and recorded at the surface the spectral response. Modelled as a sinc function, this approximate source has constant amplitude for all frequencies below a cut frequency chosen arbitrarily at 5 Hz, value allowing numerous resonance modes to be modelled and recorded at surface above the conduit. The time step is 0.0001 s and grid nodes are defined with 0.5 m spacing. Absorbing boundary conditions at the side of the domain and a free-surface condition are used like in Jousset *et al.* (2003). We computed several models with different source location. For all models, the natural frequencies of the resonator have higher amplitudes. At constant geometry (we use a dyke model having 1 km long, 10 m thick), the natural dominant frequencies of the system appear, wherever the impulsive source is located. However, amplitudes for each mode in different source location may be different as they may be excited with different amplitude depending on the position of the source. In order to excite the lowest frequency of resonance (fundamental mode) we triggered the source in the middle of the conduit. We found the period with the largest amplitude at about 10 to 30 s (Fig. 10). Note that the interface waves propagating along the interface between the brine and the salt and producing the resonance are dispersive (Chouet 1986; Jousset *et al.* 2003; Jousset *et al.* 2004; Karpfinger *et al.* 2010). We neglected the dispersion in our modelling as we focus of the order of magnitude of the resonance period.

On the basis of those over-simplified models, we suggest that the excitation frequencies of the remote earthquake waves, although of small amplitudes, may have provided vibrations with frequencies spanning values close to the natural resonance frequency of the cavern + brine overburden system. This could have contributed to amplify displacements and increase the local stress changes and trigger micro-earthquakes.

5 SUMMARY AND FURTHER WORKS

We monitored the collapse of a salt cavern with three broadband seismometers. We document for the first time in a mining environment, three types of earthquakes (brittle-like micro-earthquakes, Long Period events and Very Long Period earthquakes), similar to those recorded in volcanic or hydrothermal systems. We surmise that the existence of such similarities is due to the presence of fluid in cracks, under stress conditions.

We demonstrated that the cavern was in a critical state, prone to collapse, by modelling the stress around the cavern by means of 2D axisymmetric elastic finite-element simulations. We acknowledge the oversimplification of our modelling as plasticity, the role of fluids and the possible dynamic non-linear behaviour of the damaged overburden were not fully incorporated, and we suggest further numerical modelling investigations using for instance distinct element method (Hazzard & Young 2004).

We found that waves generated by an M∼7.2 earthquake at more than 10000 km were clearly correlated with micro-earthquake occurrence and more specifically with a dramatic increase in both number and magnitude of micro-earthquakes. We observed that micro-seismicity occurred around the cavern during the Rayleigh waves train from the remote earthquake and neither before or shortly afterwards.

We investigated the role of the exploitation channels, which may trap the seismic energy due to the impedance contrast between the brine and the surrounding rock (Chouet 1986; Neuberg 2000; Jousset *et al.* 2003). We showed that the excitation of the system is poorly explained by the only presence of fluid-filled cavern, but far better by the presence of these fluid-filled 1 km long horizontal conduits at the rear of the cavern.

Our analysis suggests that the triggering of microseismicity leading to the collapse could have been provoked by the passing waves of the remote earthquake for at least two reasons:

(1) The cavern was ready to collapse so that a slight stress increase was sufficient to trigger microseismicity;

(2) The excitation frequency was close to the resonance frequency of the fluid-filled cavern and channel, which amplified the ground response by a factor of 2 as observed compared to the expected Rayleigh wave amplitude.

This may explain why the seismicity rate increased very suddenly and sharply and did not follow a pattern like power-law accelerations described in failure forecast methods (Bell *et al.* 2011).

Both surface waves have frequencies ∼10–30 s of the same order as the natural resonance frequency. Distinguishing between contributions of Love and Rayleigh waves as main contributors to microseismicity is not straightforward. The correspondence between microearthquakes and the passage of Rayleigh waves (Fig. 6b) indicate that Rayleigh waves were the most efficient for triggering the microearthquakes. Can we identify which fractures were first initiated? This question would need investigating the relative contribution of the normal stress versus tangential stress for specific fracture planes with various dip and azimuth with respect to the direction of the propagation of the remote waves. Based on Hill (2008, 2009, 2010), we computed stresses for several crack orientation and we find that for all crack directions and dip, the largest stress contribution is the normal component for the Rayleigh wave, which is in accordance with our observation. Further analysis of the triggered swarm of microearthquakes (moment tensor analysis) may help in defining the respective role of normal and tangential components for both Love and Rayleigh waves.

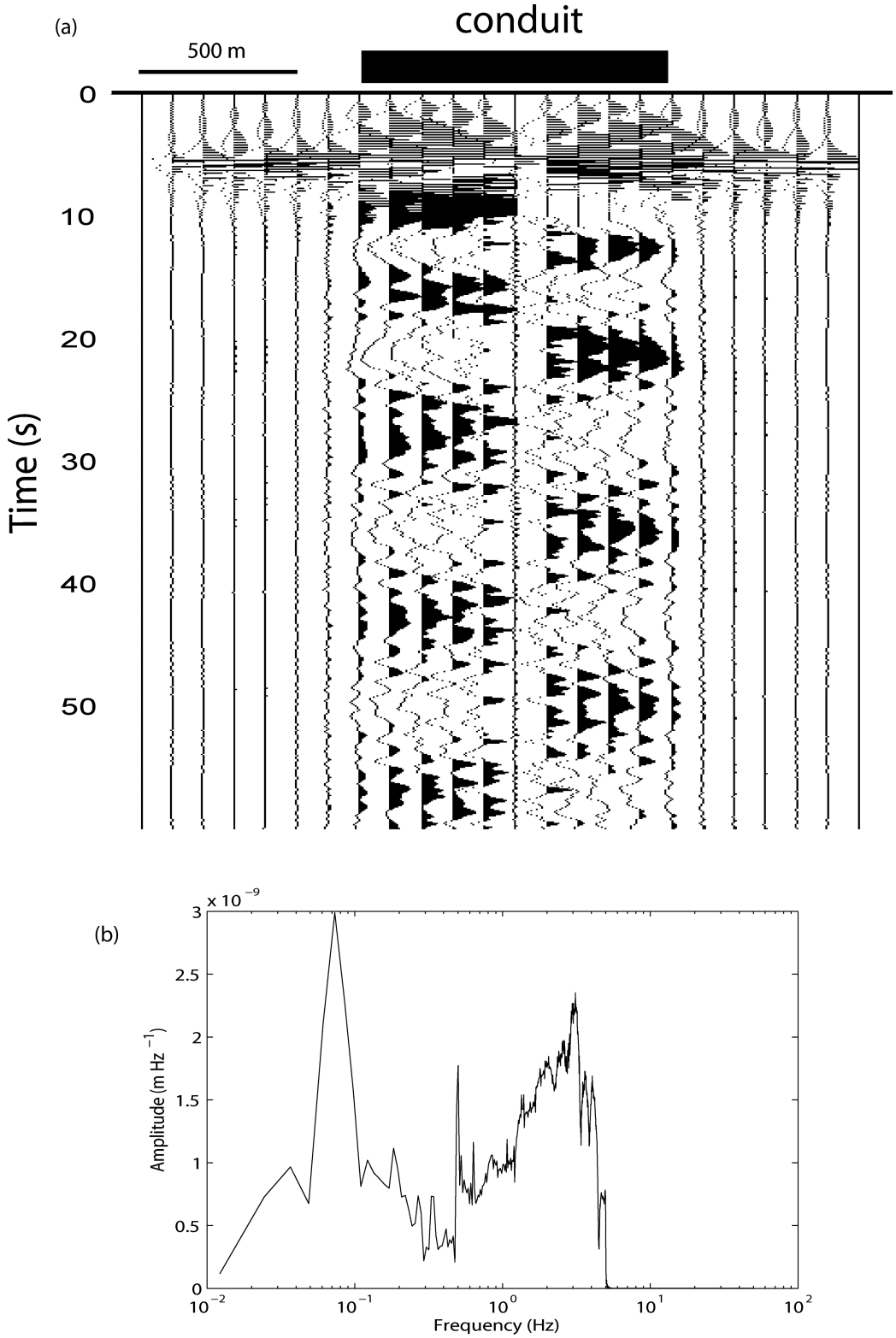

Figure 10. (a) Synthetic signals computed for an array of several virtual seismometers along the 2-D conduit; its location is indicated with the thick black line. The ultra long period of about 20 s corresponds to the fundamental frequency of the fluid-filled conduit. (b) Spectral content of the vertical component of one of the records above the conduit.

These results could be the start of new research investigations with respect to unstable systems in mining environment continuously subjected to internal fluctuations and under the threat of external forces, like natural triggering effects like earth tides (Hawthorne & Rubin 2010) or anthropogenic small perturbations (e.g. drilling activities). Evidence of highly stressed rocks in the system at Cerville-Buissoncourt was given by Lebert *et al.* 2011. They recorded precursors to the collapse in the very-high frequency

range. The relationship between these precursory signals and microseismicity remains to be examined, in particular with source mechanism of microearthquakes (Daupley *et al.* 2010; Mercerat *et al.* 2010). Studying these artificially created unstable systems may also allow gaining further understanding of the dynamics of complex out-of-equilibrium natural systems like geysers or volcanoes with pit-craters or even calderas.

ACKNOWLEDGMENTS

The authors would like to thank the Lorraine Regional Authority for its backing of the GISOS teams, the mine operating team which provided the time and facilities that made the GISOS experiments possible, and all their GISOS colleagues for continuing support and discussion both in the field and afterwards. We thank B. François for his help in setting-up the broad-band network. We acknowledge F. Lebert, A. Bitri, S. Bernardie, B. Bazargan, N. Coppo, J.C. Gourry and R. Gritto for fruitful discussions. Critical reviews by David Hill and one anonymous reviewer improved the manuscript.

REFERENCES

Amitrano, D., 2006. Rupture by damage accumulation in rocks, *Int. J. Fract.,* **139**(3–4), 369–381, doi:10.1007/s10704-006-0053-z.

Bell, A.F., Naylor, M., Heap, M.J. & Main, I.G., 2011. Forecasting volcanic eruptions and other material failure phenomena: an evaluation of the failure forecast method, *Geophys. Res. Lett.,* **38,** L15304, doi:10.1029/2011GL048155.

Brodsky, E.E. & Prejean, S.G., 2005. New constraints on mechanisms of remotely triggered seismicity at Long Valley Caldera, *J. geophys. Res.,* **110,** B04302, doi:10.1029/2004JB003211.

Bourquin, S., Vairon, J. & Le Strat, P., 1997. Three-dimensional evolution of the Keuper of the Paris basin based on detailed isopach maps of the stratigraphic cycles: tectonic influences, *Geol. Rundsch.,* **86,** 670–685.

Cannata, A., Di Grazia, G., Montalto, P., Aliotta, M., Patanè, D. & Boschi, E., 2010. Response of Mount Etna to dynamic stresses from distant earthquakes, *J. geophys. Res.,* **115,** B12304, doi:10.1029/2010JB007487.

Capozza, R., Vanossi, A., Vezzani, A. & Zapperi, S., 2009. Suppression of friction by mechanical vibrations, *Phys. Rev. Lett.,* **103,** 085502, doi:10.1103/PhysRevLett.103.085502.

Chao, K., Peng, Z., Wu, C., Tang, C.-C. & Lin, C.-H., 2011. Remote triggering of non-volcanic tremor around Taiwan, *Geophys. J. Int.,* **188,** 301–324, doi:10.1111/j.1365-246X.2011.05261.x.

Chouet, B., 1986. Dynamics of a fluid-driven crack in three dimensions by the finite difference method, *J. geophys. Res.,* **91,** 13 967–13 992.

Chouet, B., Dawson P. & Arciniega-Ceballos, A., 2005. Source mechanism of Vulcanian degassing at Popocatépetl Volcano, Mexico, determined from waveform inversions of very long period signals, *J. geophys. Res.,* **110,** B07301, doi:10.1029/2004JB003524.

Cochran E.S., Vidale, J.E. & Tanaka, S., 2004. Earth Tides can trigger shallow thrust fault earthquakes, *Science,* **306,** 1164–1166, doi:10.1126/science.1103961.

Contrucci, I., Klein, E., Cao, N.-T., Daupley, X. & Bigarré, P., 2011. Multiparameter monitoring of a solution mining cavern collapse: first insight of precursors, *C. R. Geosci.,* **343**(1), 1–10, doi:10.1016/j.crte.2010.10.007.

Daupley, X. *et al*., 2010. Multiparameter monitoring of a salt cavern collapse (Cerville-Buissoncourt site, France), *Geophys. Res. Abstracts,* **12,** EGU 2010–12404.

Di Grazia, G., Cannata, A., Montalto, P., Patanè, D., Privitera, E., Zuccarello, L. & Boschi, E., 2009. A new approach to volcano monitoring based on 4D analyses of seismo-volcanic and acoustic signals: the 2008 Etna eruption, *Geophys. Res. Lett.,* **36,** L18307, doi:10.1029/2009GL039567.

Ferrazzini, V. & Aki, K., 1987. Slow waves trapped in fluid-filled infinite-crack: implication for volcanic tremor, *J. geophys. Res.,* **92,** 9215–9223.

Ford, S.R., Dreger, D.S. & Walter, W.R., 2008. Source characterization of the 6 August 2007 Crandall Canyon mine seismic event in central Utah. *Seism. Res. Lett.,* **79**(5), 637–644, doi:10.1785/gssrl.79.5.637.

Gomberg, J., Reasenberg, P., Bodin, P. & Harris, R., 2001. Earthquake triggering by seismic waves following the Landers and Hector Mine earthquakes, *Nature,* **411,** 416–466, doi:10.1038/35078053.

Gomberg, J., 2010. Lessons from (triggered) tremor, *J. geophys. Res.,* **115,** B10302, doi:10.1029/2009JB007011.

Guilhem, A., Peng, Z. & Nadeau, R.M., 2010. High-frequency identification of non-volcanic tremor triggered by regional earthquakes, *Geophys. Res. Lett.,* **37,** L16309, doi:10.1029/2010GL044660.

Hawthorne, J.C. & Rubin, A.M., 2010. Tidal modulation of slow slip in Cascadia, *J. geophys. Res.,* **115,** B09406, doi:10.1029/2010JB007502.

Hazzard, J.F. & Young, R.P., 2004. Dynamic modelling of induced seismicity, *Int. J. Rock Mech. Min. Sci.,* **41**(8), 1365–1376, doi:10.1016/j.ijrmms.2004.09.005.

Hill, D.P., 2008. Dynamic stresses, Coulomb failure, and remote triggering, *Bull. seism. Soc. America.,* **98,** 66–92.

Hill, D.P., 2009. Erratum: Dynamic stresses, Coulomb failure and remote triggering, *Bull. seism. Soc. America.,* **99,** 2050–2051.

Hill, D.P., 2010. Surface-Wave Potential for Triggering Tectonic (Non-volcanic) Tremor, *Bull. seism. Soc. Am.,* **100**(5A), 1859–1878, doi:10.1785/0120090362.

Hill, D.P. & Prejean, S., 2007. Dynamic triggering, in *Treatise on Geophysics,* pp. 257–291, ed. Kanamori, H., Elsevier, Amsterdam.

Hough, S.E., 2005. Remotely triggered earthquakes following moderate mainshocks (or why California is not falling into the ocean), *Seism. Res. Lett.,* **76,** 58–66.

Ingebritsen, S.E. & Rojstaczer, S.A., 1996. Geyser periodicity and the response of geysers to deformation, *J. geophys. Res.,* **101**(B10), 21 891–21 905.

ISRM (International Society of Rock Mechanics), 2008. International Commission on Mine Closure — Mine closure and Post Mining Management International State of the Art, Technical Report, Available at: http://www.ineris.fr/centredoc/CDi__mineclosure_29_11_08-ang.pdf. (last accessed 2012 July).

Itaba, S. & Ryosuke, A., 2011. A slow slip event triggered by teleseismic waves, *Geophys. Res. Lett.,* **38,** L21306, doi:10.1029/2011GL049593.

Jackson, J.R., 1833. On the Seiches of Lakes, *J. R. Geogr. Soc. London,* **3,** 271–275, doi:10.2307/1797612.

Jolly, A., Neuberg, J., Jousset, P. & Sherburn, S., 2012. A new source process for evolving repetitious earthquakes at Ngauruhoe volcano, New Zealand, *J. Volc. Geotherm. Res.,* **215–216,** 26–39.

Johnson, P.A. & Jia, X., 2005. Nonlinear dynamics, granular media and dynamic earthquake triggering, *Nature,* **473,** 871–874, doi:10.1038/nature04015.

Jousset, P., Neuberg, J. & Surton, S., 2003. Modelling the time-dependent frequency content of low-frequency volcanic earthquakes, *J. Volc. Geotherm. Res.,* **128,** 201–223, doi:10.1016/S0377-0273(03)00255-5.

Jousset, P., Neuberg, J. & Jolly, A., 2004. Modelling low-frequency volcanic earthquakes in a viscoelastic medium with topography, *Geophys. J. Int.,* **159,** 776–802.

Jousset, P. & Douglas, J., 2007. Long period earthquake ground displacements recorded on Guadeloupe (French Antilles), *Earthq. Eng. Struct. Dyn.,* **36**(7), 949–963, doi:10.1002/eqe.666.

Jousset, P., Bazargan-Sabet, B., Lebert, F., Bernardie, S. & Gourry, J.-C., 2010. Geophysical observations at cavity collapse, *Geophys. Res. Astracts,* **12,** EGU 2010–4993.

Jousset, P., Haberland, C., Bauer, K. & Arnason, K., 2011. Hengill geothermal volcanic complex (Iceland) characterized by integrated geophysical observations, *Geothermics,* **40**(1), 1–24, doi:10.1016/j.geothermics.2010.12.008.

Julian, B., 1994. Volcanic tremor: non-linear excitation by fluid flow, *J. geophys. Res.,* **99**(B6), 11 859–11 877.

Karpfinger, F., Valero, H.-P., Gurevich, B., Bakulin, A. & Sinha, B., 2010. Spectral-method algorithm for modeling dispersion of acoustic modes in elastic cylindrical structures, *Geophysics,* **75,** H19–H27, doi:10.1190/1.3380590.

King, G.C.P., Stein, R.S. & Lin, J., 1994. Static stress changes and the triggering of earthquakes, *Bull. seism. Soc. Am.,* **84,** 935–953.

Kubotera, A., 1974. Volcanic tremors at Aso volcano, in *Physical Volcanology*, pp. 29–48, ed Civetta, L., Gasparini, G., Luongo, G. & Rapolla A., Elsevier, Amsterdam.

Lay, T. & Wallace, T.C., 1995. *Modern Global Seismology,* 521 pp., Academic Press, San Diego, California.

Lebert, F., Bernardie, S. & Mainsant, G., 2011. Hydroacoustic monitoring of a salt cavity: an analysis of precursory events of the collapse, *Nat. Hazards Earth Syst. Sci.,* **11,** 2663–2675, doi:10.5194/nhess-11-2663-2011.

Manga, M. & Brodsky, E., 2006. Seismic triggering of eruptions in the far field: volcanoes and geysers, *Annu. Rev. Earth planet. Sci.,* **34,** 263–291, doi:10.1146/annurev.earth.34.031405.125125.

Manga, M., Brumm, M. & Rudolph, M.L., 2009. Earthquake triggering of mud volcanoes, *Mar. Pet. Geol.,* **26,** 1785–1798, doi:10.1016/j.marpetgeo.2009.01.019.

Marsan, D. & Nalbant, S.S., 2005. Methods for measuring seismicity rate changes: a review and a study of how the Mw 7.3 landers earthquake affected the aftershock sequence of the Mw 6.1 Joshua Tree Earthquake, *Pure appl. Geophys.,* **162**(6), 1151–1185, doi:10.1007/s00024-004-2665-4.

McNutt, S.R., 2000. Seismic Monitoring, in *Chapter 68 of Encyclopedia of Volcanoes,* pp. 1095–1119, eds Sigurdsson, H., Houghton, B., McNutt, S.R., Rymer, H. & Stix, J., Academic Press, San Diego, CA.

Mercerat, E., 2007. Sismicité induite et modélisation numérique de l'endommagement dans un contexte salin, *PhD thesis*. LAEGO/INERIS/IPG, Paris, France (in French).

Mercerat, E.D., Driad-Lebeau, L. & Bernard, P., 2010. Induced seismicity monitoring of an underground Salt Cavern prone to collapse, *Pure appl. Geophys.,* **167,** 5–25, doi:10.1007/s00024-009-0008-1.

Metivier, L., de Viron, O., Conrad, C.P., Renault, S., Diament, M. & Patau, G., 2009. Evidence of earthquake triggering by the solid earth tides, *Earth planet. Res. Lett.,* **278,** 370–375.

Miyazawa, M. & Brosdky, E., 2008. Deep low-frequency tremor that correlates with passing surface waves, *J. Geotherm. Res.,* **113**(B01307), doi:10.1029/2006JB004890.

Nasseri-Moghaddam, A., Cascante, G., Phillips, C. & Hudchison, D.J., 2007. Effects of underground cavities on Rayleigh-waves – Field and numerical experiments, *Soil Dyn. Earthq. Eng.,* **27,** 300–313.

Neuberg, J., Luckett, R., Ripepe, M. & Braun, T., 1994. Highlights from a seismic broadband array on Stromboli volcano, *Geophys. Res. Lett.,* **21,** 749–752.

Neuberg, J., 2000. Characteristics and causes of shallow seismicity in andesite volcanoes, *Phil. Trans. R. Soc. Lond.,* **358,** 1533–1546.

Noda, H., Dunham, E.M. & Rice, J.R., 2009. Earthquake ruptures with thermal weakening and the operation of major faults at low overall stress levels, *J. geophys. Res.,* **114**(B07302), doi 10.1029/2008JB006143.

Nothnagel, R., 2003. Modélisation des instabilités en Mécanique des Roches: application à l'exploitation de la concession de Drouville, *PhD thesis*. École des Mines de Paris, Paris, France (in French).

Peng, Z., Vidale, J.E., Wech, A.G., Nadeau, R.M. & Creager, K.C., 2009. Remote triggering of tremor along the San Andreas Fault in central California, *J. geophys. Res.,* **114**(B00A06), doi:10.1029/2008JB006049.

Raucoules, D., Maisons, C., Carnec, C., Le Mouelic, S., King, C. & Hosford, S., 2003. Monitoring of slow ground deformation by ERS radar interferometry on the Vauvert salt mine (France): Comparison with ground-based measurement, *Remote Sens. Environ.,* **88**(4), 468–478, doi:10.1016/j.rse.2003.09.005.

Roeloffs, E., 1996. Poroelastic techniques in the study of earthquake-related hydrologic phenomena, *Adv. Geophys.,* **37,** 135–195.

Rubinstein, J.L., Gomberg, J., Vidale, J.E., Wech, A.G., Kao, H., Creager, K.C. & Rogers, G., 2009. Seismic wave triggering of nonvolcanic tremor, episodic tremor and slip, and earthquakes on Vancouver Island, *J. geophys. Res.,* **114**(B00A01), doi:10.1029/2008JB005875.

Smerzini, C., Avilés, J., Paolucci, R. & Sánchez-Sesma, F.J., 2009. Effect of underground cavities on surface earthquake ground motion under SH wave propagation, *Earthq. Eng. Struct. Dyn.,* **38**(12), 1441–1460, doi:10.1002/eqe.912.

Socoliuc, A., Gnecco, E., Maier, S., Pfeiffer, O., Baratoff, A., Bennewitz, R. & Meyer, E., 2006. Atomic-scale control of friction by actuation of nanometer-sized contacts, *Science,* **313**(5784), 207–210, doi:10.1126/science.1125874.

Surono, P. *et al*., 2012. The 2010 explosive eruption of Java's Merapi volcano – a '100-year' event, *J. Volc. Geotherm. Res.,* doi:10.1016/j.jvolgeores.2012.06.018.

Van der Elst, N.J. & Brodsky, E.E., 2010. Connecting near and farfield earthquake triggering to dynamic strain, *J. geophys. Res.,* **115,** B07311, doi:10.1029/2009JB006681.

Velasco, A.A., Hernandez, S., Parsone, T. & Pankow, K., 2008. Global ubiquity of dynamic earthquake triggering, *Nat. Geosci.,* **1,** 375–379, doi:10.1038/ngeo204.

Walter, T.R., Wang, R., Acocella, V., Neri, M., Grosser, H. & Zschau, J., 2009. Simultaneous magma and gas eruptions at three volcanoes in southern Italy: an earthquake trigger?, *Geology,* **37**(3), 251–254, doi:10.1130/G25396A.